

## Examining the Kinematic Structures within which Lightning Flashes Are Initiated Using a Cloud-Resolving Model

VICENTE SALINAS,<sup>a</sup> ERIC C. BRUNING,<sup>a</sup> AND EDWARD R. MANSELL<sup>b</sup>

<sup>a</sup> *Department of Geosciences, Atmospheric Science Group, Texas Tech University, Lubbock, Texas*

<sup>b</sup> *NOAA/OAR National Severe Storms Laboratory, Norman, Oklahoma*

(Manuscript received 10 May 2021, in final form 19 October 2021)

**ABSTRACT:** Lightning is frequently initiated within the convective regions of thunderstorms, and so flash rates tend to follow trends in updraft speed and volume. It has been suggested that lightning production is linked to the turbulent flow generated by updrafts as turbulent eddies organize charged hydrometeors into complex charge structures. These complex charge structures consist of local regions of increased charge magnitudes between which flash-initiating electric fields may be generated. How turbulent kinematics influences lightning production, however, remains unclear. In this study, lightning flashes produced in a multicell and two supercell storms simulated using The Collaborative Model for Multiscale Atmospheric Simulation (COMMAS) were examined to identify the kinematic flow structures within which they occurred. By relating the structures of updrafts to thermals, initiated lightning flashes were expected to be located where the rate of strain and rotational flow are equal, or between updraft and eddy flow features. Results showed that the average lightning flash is initiated in kinematic flow structures dominated by vortical flow patterns, similar to those of thermals, and the structures' kinematics are characterized by horizontal vorticity and vertical shearing. These kinematic features were common across all cases and demonstrated that where flash-initiating electric fields are generated is along the periphery of updrafts where turbulent eddies are produced. Careful consideration of flow structures near initiated flashes is consistent with those of thermals rising through a storm.

**KEYWORDS:** Eddies; Updrafts/downdrafts; Vertical motion; Lightning; Atmospheric electricity; Convective storms; Storm environments; Vorticity; Cloud resolving models


### 1. Background

The electrification of thunderstorms has been studied extensively in past work (Wilson 1921; Simpson and Scrase 1937; Reynolds et al. 1957; Takahashi 1978; Williams 1985; Saunders and Peck 1998). The dynamics of a storm's updraft facilitates the growth of hydrometeor species (e.g., graupel, ice, and hail), as water vapor is ingested and moved upward into a storm (Takahashi 1978; Saunders and Peck 1998; Saunders 2008). The rate of growth, collisional frequency, and number concentrations of ice hydrometeors, namely, graupel and ice, is dependent on the surrounding cloud temperature, and liquid water and water vapor content, which determines the rate of charge they acquire within a deep mixed phase region above altitudes whose temperature is less than 0°C (Takahashi 1978; Mitzewa et al. 2005). It is through these processes that a graupel-ice collisional noninductive charging mechanism (NIC) was identified as the primary means by which a storm is electrified (Takahashi 1978; Saunders 2008).

The NIC is important in establishing a storm's electrical charge structure because where hydrometeors accumulate in a storm defines the largest charge regions (Williams 1985; Stolzenburg et al. 1998). A storm's charge structure is usually defined as a tripole that consists of an upper positive, midlevel negative, and lower positive charge regions (Williams 1985). The tripole structure was defined from electric field measurements taken from thunderstorms, and determines the structure of the electric potential that is formed by accumulations of charged hydrometeors driven by a storm's flow and gravitational forces (i.e., vertical shearing and differential sedimentation; Williams and Lhermitte 1983).

However, recent studies have shown that the actual charge structure of a storm is more complex, in that it cannot be easily defined by a set number of charge layers (Stolzenburg et al. 1998; Calhoun et al. 2013; Brothers et al. 2018). Unlike the tripole depiction, which is defined by the electric potential, which smooths the distribution of charge within a storm (Bruning and MacGorman 2013), complex charge structures are defined in terms of the charge densities, and so their spatial variability is retained (Brothers et al. 2018). These charge structures were found to vary in complexity across the turbulent-convective to shear-driven-anvil regions of storms, and so it was suggested that their formation is defined by changes in the complexity of a storm's kinematic structure (Brothers et al. 2018).

How a storm's charge structure is defined is crucial for studies investigating how and why lightning is initiated (Rison et al. 2016; Iudin 2017), as how the electric fields supporting electrical breakdown are generated remains unknown

 Denotes content that is immediately available upon publication as open access.

Salinas's current affiliation: Cooperative Institute for Severe and High-Impact Weather Research and Operations, University of Oklahoma, Norman, Oklahoma.

*Corresponding author:* Vicente Salinas, vicente.salinas@noaa.gov

DOI: 10.1175/JAS-D-21-0132.1

© 2022 American Meteorological Society. For information regarding reuse of this content and general copyright information, consult the [AMS Copyright Policy](#) ([www.ametsoc.org/PUBSReuseLicenses](#)).

(Rakov and Uman 2003). Under a tripole depiction, the electric potential overgeneralizes how charge is structured, and so identification of the electric fields that initiate the smallest flashes [i.e., hundreds of meters in length; Bruning and Thomas 2015] within storms is not possible (Bruning and MacGorman 2013). Therefore, it has been suggested that the complex charge structures composed of much smaller charge regions are responsible for the generation of the spatially confined breakdown electric fields needed to initiate a lightning flash (Bruning and MacGorman 2013; Rison et al. 2016; Brothers et al. 2018).

In the present study, we seek to examine storm kinematics and kinematic flow structures within which lightning is initiated. Identification of flow structures in which lightning is initiated provides insight as to how storm kinematics may drive local hydrometeor growth, accumulations, and charging processes that are responsible for generating flash-initiating electric fields. Because it has been suggested that turbulence and lightning flash rates and sizes are directly related (Bruning and MacGorman 2013), and that the temporal changes in flash rates and sizes occur as consequence of similar changes in a storm's fluid dynamics as a storm evolves and intensifies in time (i.e., updraft volume; Deierling and Petersen 2008; Mecikalski et al. 2015; Schultz et al. 2015), we anticipate that most lightning flashes initiate in regions of a storm with similar turbulent eddy kinematic flow structures. Moreover, these eddy flow structures will depict the kinematics found along the periphery, or edge, of an updraft's maximum ascent rate, where turbulent eddies are generated (Bryan et al. 2003) and flashes are frequently initiated (DiGangi et al. 2016). We expect that because an updraft's maximum rate of ascent is transient—in that the ascent rate is pulse-like due to a transient source of positive buoyancy (Romps and Charn 2015; Hernandez-Deckers and Sherwood 2016; Morrison and Peters 2018; Peters et al. 2019)—that the initiation of lightning flashes track its ascent through the storm, and occurs where the formation of turbulent eddies is favored along its periphery. This is consistent with past works, which have suggested that lightning activity ascends as a “lightning-bubble” in storms (Ushio et al. 2003), and at a similar rate as the updraft (MacGorman et al. 2017).

We make use of The Collaborative Model for Multiscale Atmospheric Simulation (COMMAS) (Wicker and Wilhelmson 1995) to simulate lightning flashes within thunderstorms to examine the dynamics within which flashes are initiated. Furthermore, we extend our reach to thermal dynamics to seek how to interpret the flow structures in which lightning is initiated. By making use of thermal dynamics, and because high flash rates and flash extent densities are generally found around the updraft, we anticipate that the structure of storm kinematics surrounding a flash initiation resembles that of the large eddies generated along the periphery of a thermal bubble (Damiani et al. 2006; Morrison and Peters 2018; Peters et al. 2019) as illustrated in Fig. 1 and for an idealized thermal in Fig. 2, where lightning is initiated between the strain and rotation dominant flow features that define them. A thermal bubble is defined as the ascent of transient bubbles of positively buoyant air (i.e., updraft) whose structure is

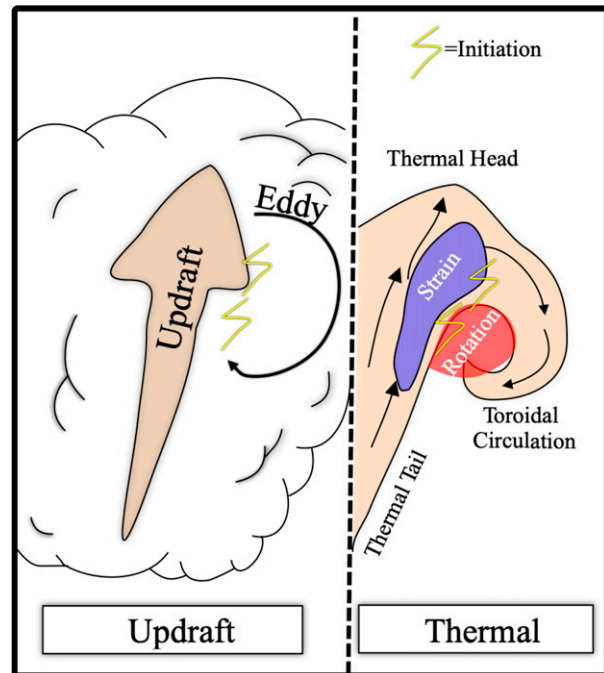


FIG. 1. Illustration of the structure of an updraft as defined by a thermal bubble. Thermal bubble structure is inspired by Fig. 3 in Morrison and Peters (2018), where the updraft may be defined by a thermal head, toroidal circulations (i.e., large eddies), and thermal tail since it does not have a continuous source of positive buoyancy. Flash initiation locations are shown between the updraft and eddy flow features, or between strain and rotation dominant flow.

defined by a thermal head, exterior toroidal circulations (i.e., large eddies), and thermal tail (Fig. 1). If such a common flow structure is identified for the average flash initiation, then we suggest this provides a clue by which future work may perform a more focused examination of how an updraft's generated eddies control the growth of ice hydrometeors that form the locally compact charge regions that have been speculated to generate the electric fields needed to initiate the smallest most frequent flashes.

## 2. Model used, cases, and simulated lightning

### a. Model overview

The National Severe Storms Laboratory's (NSSL) COMMAS was employed as it couples storm kinematics and microphysics to graupel-ice collisional noninductive and graupel-droplet inductive charging parameterizations for storm electrification (Mansell et al. 2005). A charge tendency equation, coupled to the charge budget in each category of hydrometeor, then accounts for charge advection, sedimentation, turbulent diffusion, ion drift, and lightning charge deposition contributions (Mansell et al. 2005). Simulated lightning flashes are initiated within a storm where the electric field achieves the relativistic runaway breakdown electric field threshold (RRBE) (Mansell et al. 2002, 2005; Dwyer 2005; Mansell et al.

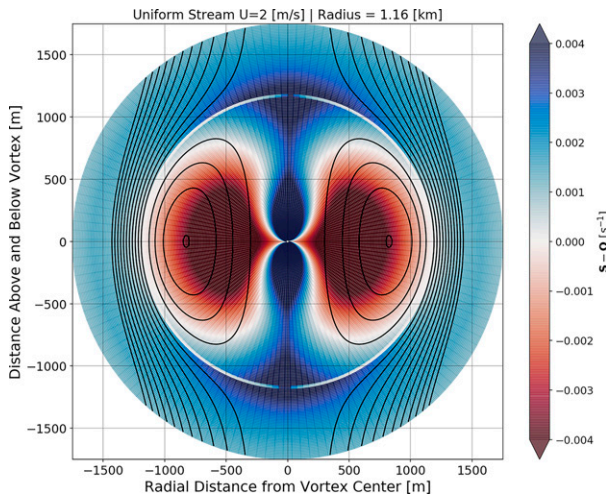


FIG. 2. Illustration of a Hills-type vortex, or ideal thermal bubble (Roms and Charn 2015; Morrison and Peters 2018), defined by a radius  $a = 1.16$  km. Velocity components are defined by  $u = U[1 - (a^3/r^3)\cos(\theta)]$  and  $v = -U[1 - (a^3/2r^3)\sin(\theta)]$  anywhere outside the bubble, and  $u = -(3/2)U[1 - (r^2/a^2)\cos(\theta)]$  and  $v = (3/2)U[1 - (2r^2/a^2)\sin(\theta)]$  inside the bubble, where  $U$  is the constant velocity of the bubble and is set to  $U = 2 \text{ m s}^{-1}$ ,  $r$  represents the radial coordinates in the domain, and  $\theta$  is each coordinates azimuth from the origin (0, 0). Black lines are defined by the streamfunction of the velocity components  $S = (1/2)U[1 - (a^3/r^2)r^2 \cos(\theta)^2]$  outside the bubble, and  $S = (1/2)U[1 - (r^2/a^2)r^2 \cos(\theta)^2]$  within it, and the red and blue color are the difference between strain and rotation tensor norms of the velocity gradient of  $u$  and  $v$ . Note that values of  $a$  and  $U$  may be selected at random as the general appearance of the flow structure remains the same.

2010; Marshall et al. 2005). RRBE is used in the model only as a reference to permit the initiation of lightning in simulated storms, and does not suggest it to be the mechanism by which actual lightning flashes are initiated.

*b. Case selection*

The selected storms included a multicell and two supercell cases. These cases were chosen to sample the kinematics across different storm modes, and storms of varying updraft intensities, to ensure that the diagnosis of storm kinematics was consistent regardless of storm type. Table 1 summarizes each case’s initialization parameters and specifications.

The three storms were simulated on domains with a uniform grid spacing of 125 m in all directions to allow the largest scale eddies to be resolved (Bryan et al. 2003), and with output time intervals every 300 s. Choice of a high spatial resolution required a coarser output time interval due to computational and storage limitations of our computing resources. However, all lightning flashes initiated within each storm were reported at their exact initiation times between model output times.

The first case (herein WK82) was simulated using the idealized Weisman and Klemp (1982) supercell with a mixed-layer convective available potential energy (CAPE) of  $3132 \text{ J kg}^{-1}$  and 0–6-km shear of  $36 \text{ m s}^{-1}$ . WK82 produced a total of 6903 flashes in a duration of 50 min when the simulation was ended.

TABLE 1. Summary of initialization specifications: WK82 and RP15 follow Brothers et al. (2018).

Specification	WK82	SL16	RP15
Domain size (km)	$60 \times 60$	$60 \times 40$	$40 \times 40$
Duration (min)	70	155	90
Temperature perturbation (K)	2	2	2
Warm bubble radius (km)	10	10	8
Mixed-layer CAPE ( $\text{J kg}^{-1}$ )	3132	5237	1881
0–6-km shear ( $\text{m s}^{-1}$ )	36	23	15

The second case (herein SL16) was simulated using a balloon-borne sounding collected for a splitting supercell storm that occurred on 22 May 2016 over the town of Slaton, Texas, and had a CAPE of  $5237 \text{ J kg}^{-1}$  and 0–6-km shear of  $23 \text{ m s}^{-1}$ . SL16 produced a total of 6280 flashes in 140 min when the simulation was ended; however, only a subset of 2878 flashes that were initiated in the right-moving cell of the storm are used as the right-moving cell maintained convection until the simulation was stopped.

The third case (herein RP15) was simulated using a balloon-borne sounding collected for a multicell storm that occurred over the town of Ropesville, Texas, on 10 July 2015, and had a CAPE of  $1881 \text{ J kg}^{-1}$  and 0–6-km shear of  $15 \text{ m s}^{-1}$ . RP15 was a much weaker storm, and produced 320 flashes during a 120-min period before the simulated storm dissipated.

For the nonidealized SL16 and RP15 cases, the shapes of the total flash rates of the simulated storms were compared to those of their real storm counterparts and were found to match; however, differences in the peak flash rates were noted (not shown). For both SL16 and RP15, the peak flash rates differed from those derived from lightning mapping array (LMA) data by a factor of 2 and 5, respectively (not shown). These differences between simulated and observed flash rates were expected as a result of the model’s idealized charging parameterizations that are sensitive to model specifications that include the grid spacing and the warm bubble initialization parameter (Brothers et al. 2018). However, that the general shapes of the flash rates were similar implies that similar electrification rates are also being captured by the simulated storms, and so we do not need the total number of flashes they produced to be exact.

*c. Simulated lightning*

Simulated lightning flash channel information was saved as collections of channel nodes. Channel nodes record the step-by-step propagation of lightning electrical breakdown (Mansell et al. 2002), and can be used to reconstruct the geometry of a lightning flash. The pre- and post-flash net charge densities are also saved at each flash point, along with the pre-flash electric potential. Bulk characteristics such as dipole moment and energy change are also calculated, but are not used in this study. Rather, we use the first channel node for each flash to identify each initiation location on the model grid.

All locations of flash initiation were grouped in relation to the model output time at which they were initiated, which was reported every 300 s. In other words, flashes initiating from

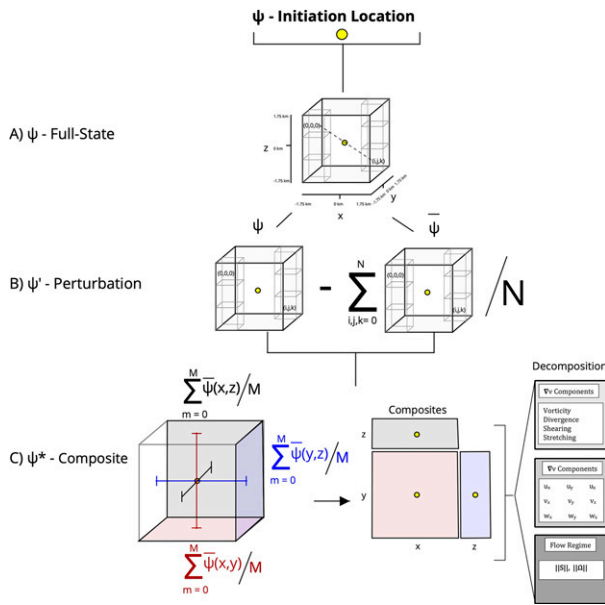


FIG. 3. Schematic of model grid term (a) base state, (b) perturbation retrieval, and (c) composites for each ( $x$ - $y$ ,  $x$ - $z$ , and  $y$ - $z$ ) planar dimension, and decomposition of initiation volume kinematics into velocity gradient and strain and rotation components. The  $\Psi$  is a placeholder variable and designates any term found within a local cubic volume around each initiation location on the model grid. For (b)  $\Psi$  represents the full storm term (unperturbed state),  $\bar{\Psi}$  is the average within the local cubic volume,  $\Psi'$  is the perturbation (local) scale, and  $N$  is the number of grid cells within the local volume by which the mean is computed, where  $N = 27000$  grid cells. For the composite flow  $\Psi_{ij}^*$ , the average flow along each planar dimension  $i, j$  is averaged for all flashes  $m$  to recover the average flow surrounding each initiation location,  $m = 1$  is the first flash index.

the beginning to end of a single model output time were assigned a unique group identifier, or group index. Thus, there was the same number of initiation groups as there are output times so as to examine the initiation locations with respect to their corresponding storm environments.

### 3. Experimental design

#### a. Computing storm generated flow

To isolate the storm generated flow  $\mathbf{v}$  from that of the environment as defined by the initial sounding, the environmental wind profile  $\mathbf{v}_e$  (homogenous at each vertical level) was subtracted from the wind at each model vertical column  $\mathbf{v}_m$  for all model output times, where the subscripts  $e$  and  $m$  denote the environmental and model velocities:

$$\mathbf{v} = \mathbf{v}_m - \mathbf{v}_e \quad (1)$$

#### b. Initiation locations, local volume subsetting, and term selection

Flash initiation locations were used to define cubic-volume (herein initiation volume) subsets of the storm environment

TABLE 2. Selected analysis terms.

Term (unit)	Symbol
Charge tendency ( $C m^{-3} min^{-1}$ )	$\rho_t$
Electric field magnitude ( $V m^{-1}$ )	$E_{bg}$
Electric potential (V)	$\phi_{bg}$
Storm velocity ( $m s^{-1}$ )	$\mathbf{v}$
Storm velocity perturbations ( $m s^{-1}$ )	$\mathbf{v}'$
Velocity gradient ( $s^{-1}$ )	$\nabla \mathbf{v}$
Perturbation velocity gradient ( $s^{-1}$ )	$\nabla \mathbf{v}'$

surrounding them (Fig. 3a). Initiation volumes were  $53.6 km^3$  and centered at each initiation location. Their width of 3.75 km (or 30 grid boxes) is the same size scale as observed updraft thermals (Damiani et al. 2006, 3–5 km). We use these subsets to identify the flow structures without having to consider the entire storm domain, thus saving on computational and storage expense, while still allowing us to look for the charge regions and large electric fields we expect near the initiation locations. These initiation volumes were used to record the storm electrostatic and kinematic terms used in this study (Table 2).

Furthermore, due to the large number of flashes produced in the entire domain for WK82, only 2032 flashes were considered as a consequence of storage and computational limitations. This subset considered every third flash in the entire flash population, and ensured that the initiation times of all flashes spanned the entirety of the simulation duration.

For the present study, the net charge tendency  $\rho_t$ , electric field magnitude  $E_{bg}$ , electric potential  $\phi_{bg}$ , storm velocity  $\mathbf{v}$ , and velocity gradient  $\nabla \mathbf{v}$  were retrieved within each initiation volume, and at each initiation location and corresponding model output time on the storm domain, where subscripts  $t$  and  $bg$  imply the net charge tendency (total of all contributors) and storm background (or full-state), respectively. Note, the electrostatic terms used are representative of an environment after all flashes have terminated between model output times, and so their magnitudes will not be on the order of electrical breakdown used in the simulation. Rather, magnitudes of the electric potential, charge tendency, and consequently the electric field, will be lower as they were largely depleted by flash activity. In addition,  $\phi_{bg}$  is expected to be small (i.e., close to zero) at the initiation locations compared to the extrema within the charge regions.

#### c. Perturbations and planar composite retrieval for analysis terms

The terms summarized in Table 2 were collected in reference to the exact locations of each flash initiation and within their initiation-volume subsets. Storm full state and perturbations were then retrieved and computed for selected terms, respectively. Full-state terms were unmodified terms within each initiation volume, and included all terms in Table 2. Perturbation terms were calculated by subtracting the average base state  $\bar{\Psi}$  within the initiation volume from the full state  $\Psi$  (Fig. 3b):

$$\Psi' = \Psi - \bar{\Psi} \quad (2)$$

where the term  $\Psi$  is a placeholder for the any term in Table 2. However, for this study, only the perturbation  $\mathbf{v}$  was computed and used to find its velocity gradient to depict the local kinematic structures and not that of the base-state flow.

Flow structures were identified by computing flow composites (Fig. 3c). The composite of a term  $\Psi_{i,j}^*$  was found by averaging it along each direction of an initiation volume, and for all flashes in a single case:

$$\Psi_{i,j}^* = \sum_{m=1}^M \left[ \sum_{k \neq i,j}^N \Psi_{m,i,j,k} / N \right] / M = \sum_{m=1}^M \bar{\Psi}_{m,i,j} / M, \quad (3)$$

where  $N$  is the number of grid cells in the local cubic volume,  $m$  is the flash number, and  $M$  are the number of flashes for a selected case. The subscripts  $i, j$  in Eq. (3) represent the two dimensions that are averaged along  $k$ , where in this instance  $i, j$  can be replaced by  $(i, j)$ ,  $(i, k)$ , or  $(j, k)$ , depicting the averages along those axes.

#### d. Storm kinematics and velocity gradient

The kinematics of a storm are defined by the velocity gradient tensor  $\nabla \mathbf{v}$ , and decomposed into its symmetric rate of strain  $\mathbf{S}$  and rotation  $\mathbf{\Omega}$  tensor components:

$$\nabla \mathbf{v} = \mathbf{S} + \mathbf{\Omega}, \quad (4)$$

and was used to quantify and diagnose the appearance of the flow structures within which lightning was initiated. Quantification of flow structures is possible by decomposing  $\mathbf{S}$  and  $\mathbf{\Omega}$  into their respective components of shearing, vorticity, stretching, and divergence (Okubo 1970; Schielicke et al. 2016):

$$\mathbf{S} = \frac{1}{2} \begin{pmatrix} 2u_x & (u_y + v_x) & (u_z + w_x) \\ (v_x + u_y) & 2v_y & (v_z + w_y) \\ (w_x + u_z) & (w_y + v_z) & 2w_z \end{pmatrix}, \quad (5)$$

$$\mathbf{\Omega} = \frac{1}{2} \begin{pmatrix} 0 & (v_x - u_y) & (u_z - w_x) \\ -(v_x - u_y) & 0 & (v_z - w_y) \\ -(u_z - w_x) & -(v_z - w_y) & 0 \end{pmatrix}. \quad (6)$$

The subscripts in both Eqs. (5) and (6) signify the direction of differentiation, and variables  $u, v$ , and  $w$  are the velocity vector components. With this information, it was possible to identify the exact kinematics that formed the structure of the flow, and allowed for examining whether similar kinematics were common across all cases.

#### e. Flow-type summarization and flow structure identification

The velocity gradient tensor components, Eqs. (5) and (6), were used to identify the dominant flow regime within which the average flash is initiated. By computing the tensor norms of the strain  $\mathbf{S}$  and rotation  $\mathbf{\Omega}$  tensors, it was possible to diagnose whether flashes typically initiate within strain or rotation dominant flow, or where their magnitudes were equal, which implies a region between vortical and strained flow structures.

The tensor norms are computed by taking the square root of the trace of each tensor multiplied by its transpose, giving the following result (Schielicke et al. 2016):

$$\|\mathbf{S}\| = \sqrt{\left(\frac{S_{11}}{2}\right)^2 + \left(\frac{S_{22}}{2}\right)^2 + \left(\frac{S_{33}}{2}\right)^2 + S_{12}^2 + S_{13}^2 + S_{23}^2}, \quad (7)$$

$$\|\mathbf{\Omega}\| = \sqrt{\Omega_{12}^2 + \Omega_{13}^2 + \Omega_{23}^2}, \quad (8)$$

where subscripts denote the tensor component along a row and column index. For example  $S_{12}$  signifies the first row and second column of the strain tensor matrix. Equations (7) and (8) were used to identify the dominant flow regime by subtracting  $\|\mathbf{S}\|$  by  $\|\mathbf{\Omega}\|$ :

$$\|\mathbf{S}\| - \|\mathbf{\Omega}\| = \begin{cases} \text{Strain dominant} & > 0 \\ \text{Pure shear} & \approx 0 \\ \text{Rotation dominant} & < 0. \end{cases} \quad (9)$$

If a flash was initiated where  $\|\mathbf{S}\| - \|\mathbf{\Omega}\|$  is either  $>0$  or  $<0$ , then its location is embedded within strain or rotational flow, respectively. Otherwise, if  $\|\mathbf{S}\| - \|\mathbf{\Omega}\| \approx 0$ , then a flash is initiated in an interstitial region between strong strain and rotational flow, where fluctuations of  $\|\mathbf{S}\|$  and  $\|\mathbf{\Omega}\|$  are small, and when averaged, will be the same [Eq. (9)].

Use of Eq. (9), in conjunction with Eq. (4), allows for both identification of the dominant components responsible for forming any and all kinematic structures, while also making their appearance comparable to those of thermal bubbles by identifying the dominant strain and rotation flow regimes at each initiation location and within their volume subsets (Fig. 1).

#### f. Initiation and output time offsets and subsetting

After carefully checking the conventions used to mark flash and model output times, flashes were tagged with a time offset with respect to the closest model output time (Fig. 4). We remind the reader here that each output time interval depicts the storm 300 s after it is written, or after all flashes have terminated in that time step.

Flashes occurring before a model output time, with  $\Delta t < 0$ , are associated with the model state as it evolved after the flash, and are termed pre-output flashes. A rising thermal bubble should appear above the flash initiation positions in these composites. For flashes  $-60 < \Delta t < 0$  s, a rising thermal bubble would be closer to the initiation position than for those more than 60 s prior. This is because the model output corresponds to flashes initiating at times closest to the representative storm environment at that time.

Flashes occurring after a model output time, with  $\Delta t > 0$ , are associated with the model state prior to the flash, and are termed post-output flashes. A rising thermal bubble should appear below the flash initiation positions in these composites. For flashes  $0 < \Delta t < 60$  s, the thermal bubble would be closer to the initiation position.

For each case, the closest 45 flashes on either side of each model output time were selected to increase the number of

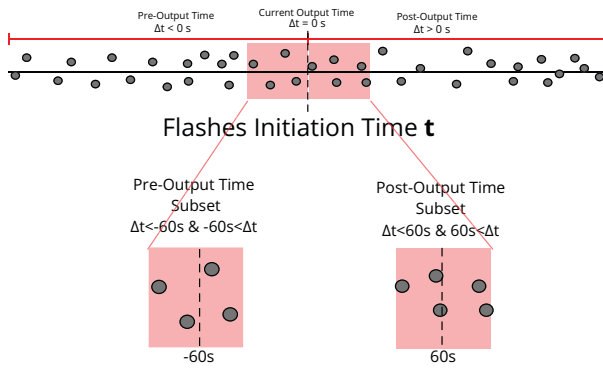


FIG. 4. Time-lag schematic for pre- and post-output time subset retrievals. Red boxes reference a subset falling within 60 s after or before a pre- and post-output environments, respectively; black dots indicate hypothetical initiations; and the  $x$  axis depicts time.

samples in both pre- and post-output subsets. The total number of flashes is summarized in the first row of Table 3. The population of 45 flashes was further subdivided into flashes within 60 s on either side of the model output time, and the pre- and post-output flash counts within 60 s are summarized in the other two rows of Table 3. The choice of using 45 flashes to subset each model output time's flash populations was arbitrary, but did confirm that all flashes that were initiated within a minute of each output time were considered while also allowing for consideration of flashes initiating  $\Delta t > 60$  s from the output time.

Inclusion of flashes initiating  $\Delta t > 60$  s  $> \Delta t$  was important in assessing the effect of flash-relative output lag on the accuracy of the kinematic composites and to check for motion consistent with a rising thermal bubble, the composites were calculated for the pre- and post-flash populations with  $\Delta t$  both greater than and less than 60 s.

#### 4. Summary of analysis methods

##### a. Initiation kinematics analysis

Storm kinematics were examined at the exact flash initiation locations for each storm, and compared to the electrostatic terms  $\rho_b$ ,  $E_{bg}$ , and  $\phi_{bg}$ . These terms were retrieved only at the model grid point that a flash was initiated and do not consider values that extend beyond it. By defining the kinematics as the rate of strain  $\|\mathbf{S}\|$  and rotation  $\|\mathbf{\Omega}\|$  tensor norms, the flow regime within which most flashes initiated, and how the corresponding electrostatics changed in relation to the dominant flow regime and flow magnitude, could be identified.

The distribution of electrostatic values for all flashes were assessed in a log-scaled  $\|\mathbf{S}\|$  and  $\|\mathbf{\Omega}\|$  parameter space. The

TABLE 3. Summary of pre- and post-output flash counts.

No. of flashes	WK82	SL16	RP15
Pre-output total	477	501	224
Post-output total	477	558	224
Pre-output $ \Delta t  < 60$ s	318	242	65
Post-output $ \Delta t  < 60$ s	327	354	63

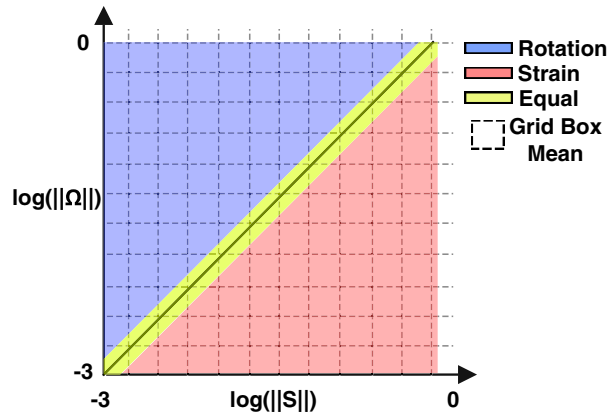


FIG. 5. Illustration of the initiation kinematics analysis parameter space for individual flash initiation locations. The  $x$  and  $y$  axes are defined by the log-scaled rate of strain and rotation tensor norms binned in increments of 50 from  $10^{-3}$  to  $10^0$   $s^{-1}$ , each grid box represents where the average of an electrostatic field is computed, and the color-filled regions signify the three flow regimes: red and blue are for strain- and rotation-dominant flow, and yellow is where their magnitudes are nearly equal as computed by  $\|\mathbf{\Omega}\|/\|\mathbf{S}\| = 1 \pm 0.01$ .

magnitudes of  $\|\mathbf{S}\|$  and  $\|\mathbf{\Omega}\|$  were binned into 50 values along each parameter space axis, ranging from  $10^{-3}$  to  $10^0$   $s^{-1}$  (Fig. 5). The average of each electrostatic term was then computed within each bin to diagnose how their changes, in relation to where flashes were initiated, coincided with changes in the magnitudes of strain and rotation flow, and in what flow regime these electrostatics resided. In addition, the total flash initiation counts were used to identify the most common flow regime in which most flashes initiated. The parameter space was divided into three regimes, a strain and rotation dominant regime identified by the ratios of  $\|\mathbf{\Omega}\|/\|\mathbf{S}\|$  of  $< 0.99$  and  $> 1.01$ , respectively; and one that reflects their equivalency along a 1:1 line where their ratio was between values of 0.99 and 1.01. These ratios define the kinematic vorticity number, which is used to identify vortex structures in synoptic (Schielicke et al. 2016) and mesoscale (Dahl 2020) storm systems.

##### b. Flow structure analysis—Flow composites

Flow composites expand upon the initiation kinematics analysis, however, electrostatic terms are no longer considered here as its sole purpose is to only identify kinematic structures. By examining the kinematics surrounding a flash initiation, a more complete depiction of what the flow looked like could be identified, and what components of the flow typically produced any and all flow structures could be extracted using the velocity gradient tensor.

The flow structures were identified by generating flow composites, as discussed in section 3c (Fig. 3c). The composites were made along the  $x$ - $z$ ,  $y$ - $z$ , and  $x$ - $y$  planes to get a 3D sense of what the flow looked like along each direction of the initiation volume. Furthermore, we average across all flashes analyzed to identify if a common flow structure is shared across an entire flash population. The flow within the flash-averaged initiation volumes were then examined in terms of

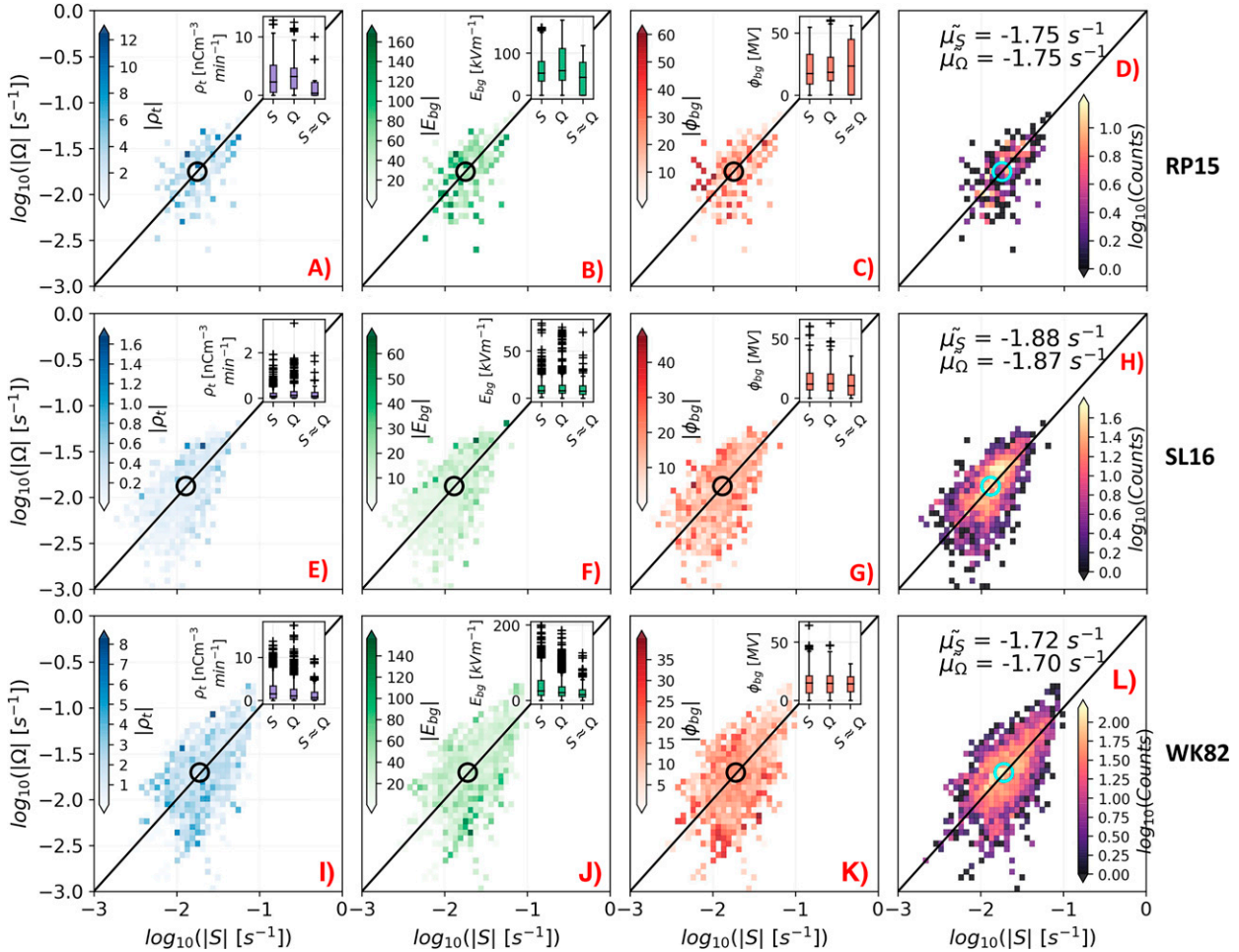


FIG. 6. Kinematic  $\|\mathbf{S}\|$  and  $\|\mathbf{\Omega}\|$  parameter space for all analyzed flashes for (a)–(d) RP15, (e)–(h) SL16, and (i)–(l) WK82. Colored fields represent the (a),(e),(i) net charge tendency  $\rho_t$  ( $\text{nC m}^{-3} \text{min}^{-1}$ ); (b),(f),(j) electric field  $E_{bg}$  ( $\text{kV m}^{-1}$ ); (c),(g),(k) electric potential  $\phi_{bg}$  (MV); and (d),(h),(l) flash counts per pixel. Inset boxes depict the distribution of electrostatic fields in regions of the parameter space dominated by  $\|\mathbf{S}\|$ ,  $\|\mathbf{\Omega}\|$ , or where they are approximately equal, the diagonal line shows where both tensors are equal in magnitude, and the black and cyan circles illustrate the median  $\|\mathbf{S}\|$ ,  $\|\mathbf{\Omega}\|$  for all flashes in the parameter space.

the components of shearing, vorticity, divergence, and stretching components, and the individual components of the velocity gradient, to identify the dominant kinematic component that formed the main flow patterns in a flow structure. Furthermore, composites of  $\|\mathbf{S}\| - \|\mathbf{\Omega}\|$  were computed to spatially identify where strain and rotation flows dominated surrounding the average initiated flash, and where a difference of 0 typically fell within the flow structures.

### 5. Results: Initiation kinematics and electrostatics

#### a. All flashes

Electrostatic terms  $\rho_t$ ,  $E_{bg}$ , and  $\phi_{bg}$  sampled at each initiated flash location were found to vary with respect to  $\|\mathbf{S}\|$  and  $\|\mathbf{\Omega}\|$ . Figure 6 shows where the largest and smallest values resided relative to large and small kinematic

magnitudes for RP15 (Figs. 6a–d), SL16 (Figs. 6e–h), and WK82 (Figs. 6i–l). In addition, values of the electrostatic terms were subdivided into separate distributions in order identify within what flow regime they resided. These flow regimes were defined by  $\|\mathbf{S}\|$  or  $\|\mathbf{\Omega}\|$  dominant flow, or where  $\|\mathbf{S}\| \approx \|\mathbf{\Omega}\|$  (inset boxes Fig. 6).

The net charge tendency  $\rho_t$  (Figs. 6a,e,i), electric field  $E_{bg}$  (Figs. 6b,f,j), and potential  $\phi_{bg}$  (Figs. 6c,g,k) showed a few consistent patterns in the kinematic parameter space, which demonstrated that changes in their magnitudes either increased or decreased with increasing or decreasing  $\|\mathbf{S}\|$  and  $\|\mathbf{\Omega}\|$ . For all cases,  $\rho_t$  and  $E_{bg}$  either increased or decreased in magnitude with increasing  $\|\mathbf{S}\|$  or  $\|\mathbf{\Omega}\|$ , where the lowest magnitudes were generally found where  $\|\mathbf{S}\| \approx \|\mathbf{\Omega}\|$ . The largest values were found in either  $\|\mathbf{S}\|$  or  $\|\mathbf{\Omega}\|$  dominant regions of the parameter space. However,  $\phi_{bg}$  was more variable for all cases (Figs. 6c,g,k). The largest values of  $\phi_{bg}$  were sampled

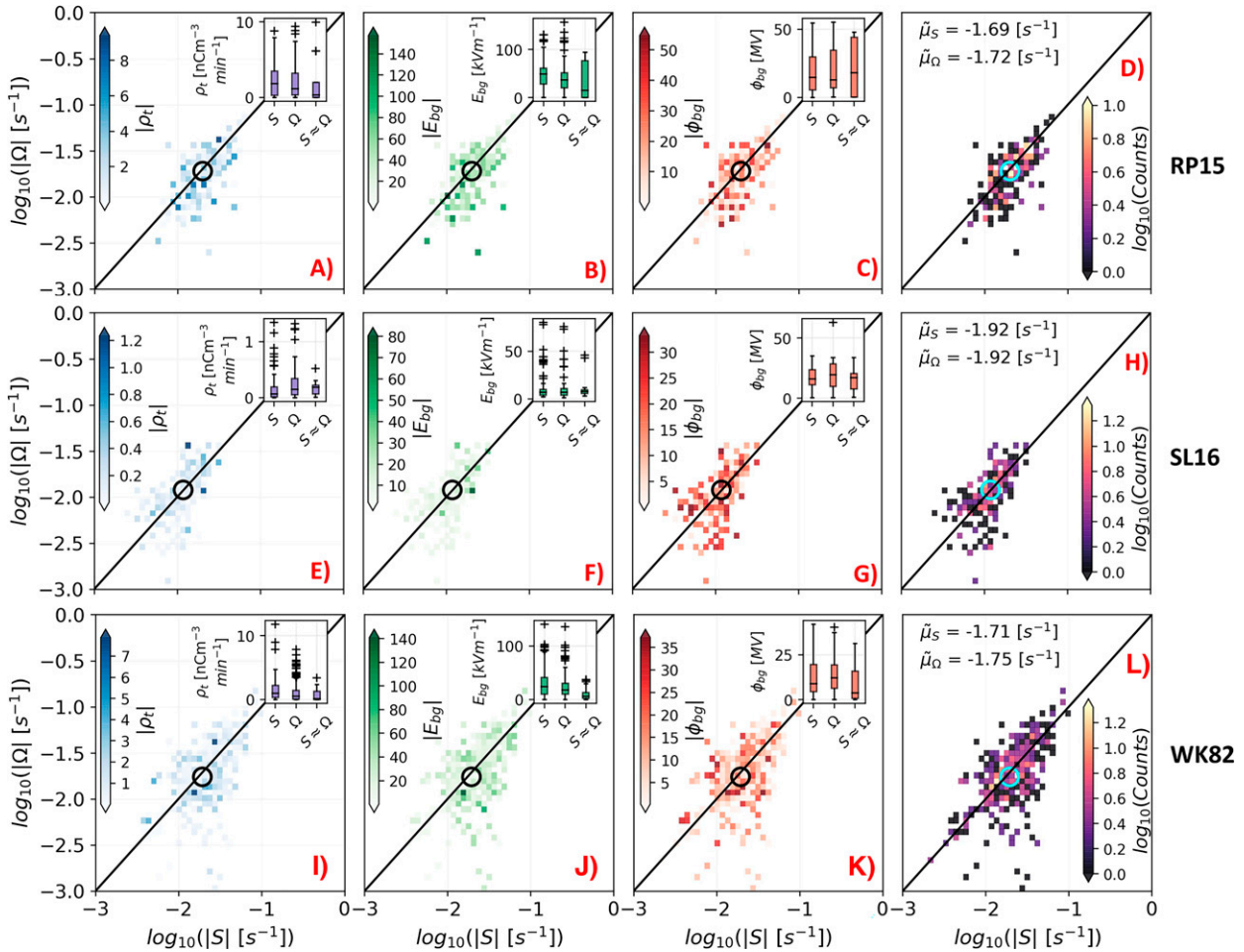


FIG. 7. Kinematic  $\|\mathbf{S}\|$  and  $\|\mathbf{\Omega}\|$  parameter space for pre-output flashes for (a)–(d) RP15, (e)–(h) SL16, and (i)–(l) WK82. Colored fields represent the (a),(e),(i) net charge tendency  $\rho_t$  ( $\text{nC m}^{-3} \text{min}^{-1}$ ); (b),(f),(j) electric field  $E_{bg}$  ( $\text{kV m}^{-1}$ ); (c),(g),(k) electric potential  $\phi_{bg}$  (MV); and (d),(h),(l) flash counts per pixel. Inset boxes depict the distribution of electrostatic fields in regions of the parameter space dominated by  $\|\mathbf{S}\|$ ,  $\|\mathbf{\Omega}\|$ , or where they are approximately equal, the diagonal line shows where both tensors are equal in magnitude, and the black and cyan circles illustrate the median  $\|\mathbf{S}\|$ ,  $\|\mathbf{\Omega}\|$  for all flashes in the parameter space.

in various parts of the kinematic parameter space, and showed that large and small values resided in either large and small magnitudes of  $\|\mathbf{S}\|$  or  $\|\mathbf{\Omega}\|$ , or where they were nearly equal (i.e., along the 1:1 line in the parameter space in Figs. 6c,g,k).

Distributions of the electrostatic terms further revealed that the largest magnitudes of  $\rho_t$  and  $E_{bg}$  for all cases resided in flow regimes dominated by  $\|\mathbf{S}\|$  and  $\|\mathbf{\Omega}\|$  (inset boxes Figs. 6a,b,e,f,i,j). The lowest  $\rho_t$  and  $E_{bg}$  resided mostly where  $\|\mathbf{S}\| \approx \|\mathbf{\Omega}\|$  as also shown by their distributions in the kinematic parameter space. However,  $\phi_{bg}$  was similarly distributed across all flow regimes (Figs. 6c,g,k). The similar distributions of  $\phi_{bg}$  in each flow regime showed that regardless of what type of kinematic field it was sampled in, its magnitude was nearly the same (inset boxes Figs. 6c–k).

The initiation counts in the parameter space were similar for all cases (Figs. 6d,h,l). The largest counts (orange-yellow colors) fell near or along the one-to-one line, which denotes where

$\|\mathbf{S}\| \approx \|\mathbf{\Omega}\|$ , and coincided with the median values of  $\|\mathbf{S}\|$  and  $\|\mathbf{\Omega}\|$  for each case's flash distribution. For RP15, the initiations tended to be most frequently sampled where both  $\|\mathbf{S}\|$  and  $\|\mathbf{\Omega}\|$  had median values of  $10^{-1.75} \text{ s}^{-1}$ , for SL16 where both  $\|\mathbf{S}\|$  and  $\|\mathbf{\Omega}\|$  had median values of  $10^{-1.88}$  and  $10^{-1.87} \text{ s}^{-1}$ , respectively, and for WK82 where  $\|\mathbf{S}\|$  and  $\|\mathbf{\Omega}\|$  had median values of  $10^{-1.72}$  and  $10^{-1.70} \text{ s}^{-1}$ , respectively (black markers Figs. 6d,h,l). This result implies that regardless of storm mode, flashes tend to initiate most frequently in flow structures between strain and rotation dominant flow regimes on the edges of the thermal updrafts (see Fig. 1).

### b. Pre-output flashes

The electrostatic and kinematic terms compared for all flashes were examined for the pre-output subsets (Fig. 7). Because fewer flashes were considered in these subsets, changes in the electrostatic and kinematic magnitudes in the



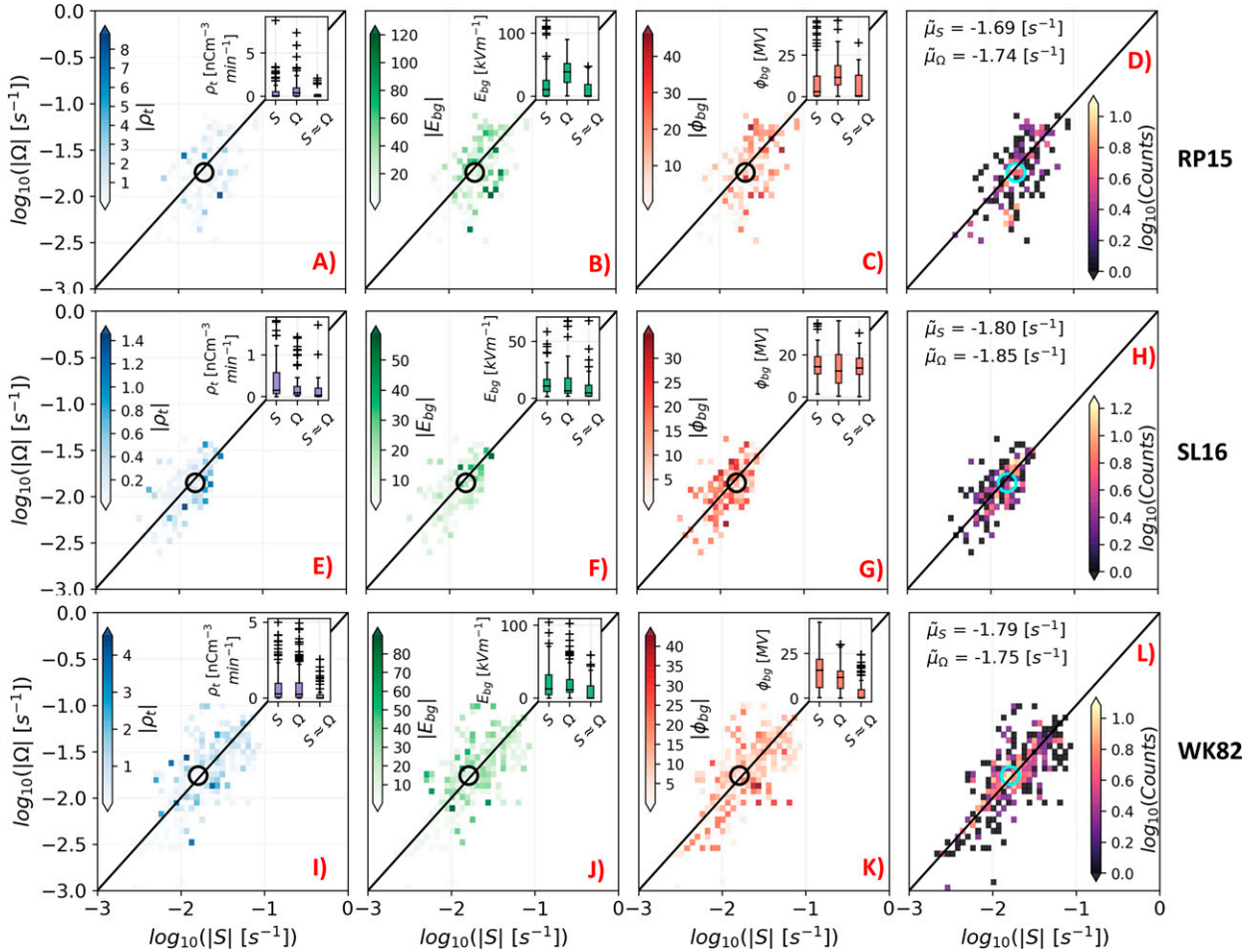


FIG. 8. Kinematic  $\|\mathbf{S}\|$  and  $\|\mathbf{\Omega}\|$  parameter space for post-output flashes for (a)–(d) RP15, (e)–(h) SL16, and (i)–(l) WK82. Colored fields represent the (a),(e),(i) net charge tendency  $\rho_t$  ( $\text{nC m}^{-3} \text{min}^{-1}$ ); (b),(f),(j) electric field  $E_{bg}$  ( $\text{kV m}^{-1}$ ); (c),(g),(k) electric potential  $\phi_{bg}$  (MV), and (d),(h),(l) flash counts per pixel. Inset boxes depict the distribution of electrostatic fields in regions of the parameter space dominated by  $\|\mathbf{S}\|$ ,  $\|\mathbf{\Omega}\|$ , or where they are approximately equal, the diagonal line shows where both tensors are equal in magnitude, and the black and cyan circles illustrate the median  $\|\mathbf{S}\|$ ,  $\|\mathbf{\Omega}\|$  for all flashes in the parameter space.

parameter space are less distinct, but remained similar to those found using all flashes.

Values of  $\rho_t$  (Figs. 7a,e,i),  $E_{bg}$  (Figs. 7b,f,j), and  $\phi_{bg}$  (Figs. 7c,g,k) showed no consistent pattern increase or decrease with  $\|\mathbf{S}\|$  or  $\|\mathbf{\Omega}\|$ . Most values of  $\rho_t$  and  $E_{bg}$  were relatively lower in magnitude than the less frequently sampled larger values that were found to reside in various flow regimes and flow magnitudes. Sampled values of  $\phi_{bg}$ , however, were much larger throughout the parameter space, existing in large and small magnitudes of  $\|\mathbf{S}\|$  or  $\|\mathbf{\Omega}\|$ , and where they were equal (i.e., along the 1:1 line in the parameter space in Figs. 7c,g,k).

Distributions of  $\rho_t$  and  $E_{bg}$  showed that the largest magnitudes were either in flow regimes dominated by  $\|\mathbf{S}\|$  or  $\|\mathbf{\Omega}\|$ , with the lowest values where  $\|\mathbf{S}\| \approx \|\mathbf{\Omega}\|$  (inset boxes Figs. 7a,b,e,f,i,j). However,  $\phi_{bg}$  was found to be similarly distributed within all flow regimes, varying less across each than for  $\rho_t$  and  $E_{bg}$  suggesting that regardless of in which flow regime

initiations were sampled in, the magnitude of  $\phi_{bg}$  was always similar.

The total initiation counts for all cases revealed that most flashes were initiated where  $\|\mathbf{S}\| \approx \|\mathbf{\Omega}\|$ , decreasing in frequency in either  $\|\mathbf{S}\|$  or  $\|\mathbf{\Omega}\|$  dominant flow (Figs. 7d,h,l). The largest initiation counts (orange–yellow colors) coincided with median values of  $\|\mathbf{S}\|$  and  $\|\mathbf{\Omega}\|$  flow, where for RP15 the median values were  $\|\mathbf{S}\| = 10^{-1.69}$  and  $\|\mathbf{\Omega}\| = 10^{-1.72} \text{ s}^{-1}$ , for SL16  $\|\mathbf{S}\| = 10^{-1.92}$  and  $\|\mathbf{\Omega}\| = 10^{-1.92} \text{ s}^{-1}$ , and for WK82  $\|\mathbf{S}\| = 10^{-1.71}$  and  $\|\mathbf{\Omega}\| = 10^{-1.75} \text{ s}^{-1}$ .

### c. Post-output flashes

The post-output initiation kinematics and electrostatics are shown in Fig. 8. As shown for the pre-output flashes, for all cases  $\rho_t$  and  $E_{bg}$  were found to be largest most frequently within  $\|\mathbf{S}\|$  and  $\|\mathbf{\Omega}\|$  dominant flow, and varied through large and small magnitudes of  $\|\mathbf{S}\|$  or  $\|\mathbf{\Omega}\|$  (Figs. 8a,b,e,f,i,j). However,  $\phi_{bg}$  varied similarly values of  $\phi_{bg}$  were consistent in

magnitude in that values sampled at each initiation location varied by less than an order of magnitude.

Distributions of  $\rho_r$  and  $E_{bg}$  showed that their largest values were sampled in either  $\|\mathbf{S}\|$  or  $\|\mathbf{\Omega}\|$  flow regimes. This was shown by both the larger spread in their distributions, or by their larger populations of outliers extending into larger magnitudes (inset boxes Figs. 8a,b,e,f,i,j).  $\phi_{bg}$  varied similarly to  $\rho_r$  and  $E_{bg}$  in the parameter space and showed the largest magnitudes were within flow regimes dominated by  $\|\mathbf{S}\|$  or  $\|\mathbf{\Omega}\|$  (e.g., Figs. 8c,k), or were the same across all three (e.g., Fig. 8g). Regardless of these changes, however, differences in  $\phi_{bg}$  were within a single order of magnitude across all flow regimes, unlike those of  $E_{bg}$ , which varied more. As found for the pre-output subsets, and for all flashes, this result demonstrates that regardless of within what flow regime an initiation was reported in, and in what magnitude of  $\|\mathbf{S}\|$  and  $\|\mathbf{\Omega}\|$  it was found, sampled values of  $\phi_{bg}$  changed little with the flow.

Total initiation counts were the largest where  $\|\mathbf{S}\| \approx \|\mathbf{\Omega}\|$  for all cases, indicating that most flashes tended to initiate somewhere between strain and rotation dominant flow kinematic structures (Figs. 8d-l). However, an exception is noted for RP15, in that an additional maximum was in strain dominant flow. The largest counts of initiations (orange and yellow colors) coincided with the median values of  $\|\mathbf{S}\|$  and  $\|\mathbf{\Omega}\|$  magnitudes that were nearly equivalent:  $10^{-1.69}$  and  $10^{-1.74} \text{ s}^{-1}$  for RP15,  $10^{-1.80}$  and  $10^{-1.85} \text{ s}^{-1}$  for SL16, and  $10^{-1.79}$  and  $10^{-1.75} \text{ s}^{-1}$  for WK82, respectively.

## 6. Results: Flow composites and kinematic structures

### a. All flashes

Flow composites revealed the kinematic structures in which flashes were initiated (Fig. 9). Figure 9 shows the kinematic structures for the base-state and perturbed flow (streamlines), and flow regime ( $\|\mathbf{S}\| - \|\mathbf{\Omega}\|$ ) on each plane. For all discussion herein, we define vortical flow as the vortex flow features shown by the velocity streamlines while rotational flow  $\|\mathbf{\Omega}\|$  implies flow dominated by the rotation component of the velocity gradient tensor.

For all cases, the base-state flow was from  $-x$  to  $+x$ , and upward from  $-z$  to  $+z$  through the initiation origin. However, variation in the flow existed along the  $y-z$  plane, where for RP15 the flow was dominated by  $+w$  with vortical flow found along the  $-y$  direction, for SL16 vortical flow was found along the  $+z$  direction, and for WK82 the flow was from negative to positive  $y$  and  $z$  directions (Figs. 9a-e).

The perturbed flow showed different flow structures as the average base-state flow direction was removed (Figs. 9b-f). For all cases, a vortical flow structure was found in the  $x-z$  plane, with strong positive vertical motion to the left of the initiation origin, and more vortical flow to the right with the average flash initiating where  $\|\mathbf{S}\| \approx \|\mathbf{\Omega}\|$ . In the  $x-y$  plane, the composite flow structure was also similar across all cases with the initiation origin centered between vortical flow structures, and where  $\|\mathbf{S}\| - \|\mathbf{\Omega}\|$  was close to a value of 0. However, along the  $y-z$  plane, the flow structures were found to differ. For RP15, the average flash was found to initiate

between two vortical flow structures, for SL16 a single vortical flow feature was found, and for WK82 a divergence flow boundary was found to be centered at the initiation origin.

The velocity gradient components were then examined within the average initiation volumes, and were used to diagnose the components of the kinematics, which formed the perturbation composite flow structures in Fig. 9, and to examine if similar kinematics could be attributed to their formation across all cases (Fig. 10). For all cases, the flow structures were found to be formed by components of horizontal vorticity and vertical shearing (Figs. 10a,d,g), with the largest contributing components dominating along the  $x-z$  and  $y-z$  planes. For RP15, vorticity made up the largest kinematic component of the velocity gradient, and was attributed to the formation of the single vortex structure along the  $x-z$  plane, and the double counterrotating vortices in the  $y-z$  plane. For SL16, the dominant components were similar, although with the addition of strong vertical shearing as well, as shown by the horizontal elongation of the vortex structures along each vertical plane. For WK82, horizontal shearing contributed to the formation of the single vortex feature along the  $x-z$  plane, but vertical divergence dominated along the  $y-z$  direction.

Further decomposition revealed that the individual velocity gradient components were either dominated by horizontal shearing of  $w$ , or vertical shearing of  $u$  and  $v$  (Figs. 10b,e,h). Therefore, the exact velocity gradients responsible for forming the composite flow structures were identified and found to be similar across all cases.

The sample distributions  $\|\mathbf{S}\|$  and  $\|\mathbf{\Omega}\|$  were also similar, such that  $\|\mathbf{S}\| \approx \|\mathbf{\Omega}\|$  on average (Fig. 10c,f,i). In comparison to values of  $\|\mathbf{S}\|$  and  $\|\mathbf{\Omega}\|$  reported in the kinematics analysis, medians of  $\|\mathbf{S}\|$  and  $\|\mathbf{\Omega}\|$  were larger than those at the exact initiation locations, implying that flashes initiated at a local minimum in strain and rotational flow are consistent with their locations being where  $\|\mathbf{S}\| \approx \|\mathbf{\Omega}\|$ . In addition, the median of each distribution for all cases were offset by the same amount by which the medians differed in the kinematics analysis (red markers), such that  $\|\mathbf{S}\|$  and  $\|\mathbf{\Omega}\|$  differed by 0.00, 0.02, and 0.03 for RP15, SL16, and WK82, respectively. The similarity between  $\|\mathbf{S}\| \approx \|\mathbf{\Omega}\|$  distributions to the values found at the exact initiation locations show that the average flash tends to initiate in kinematic structures that straddle between dominant vortex and sheared flow, as was identified in Fig. 9. Note that more variation in  $\|\mathbf{S}\| \approx \|\mathbf{\Omega}\|$  in Fig. 9, however, can be attributed to the velocity gradient being much weaker for RP15 and SL16 storms in comparison to WK82, and so the initiation average tends to have less of a coherent structure than what the streamlines depict in Fig. 9.

### b. Pre-output flashes

Composites for the pre-output subsets were examined only along vertical planes in the  $x$  and  $y$  directions to identify if their structures resembled those of thermals. For these subsets, flashes that were initiated with a  $\Delta t$  either  $<60$  s or  $>60$  s from the model output times were looked at separately to determine the importance of accounting for the initiation time lag on how the flow is structured surrounding them. In

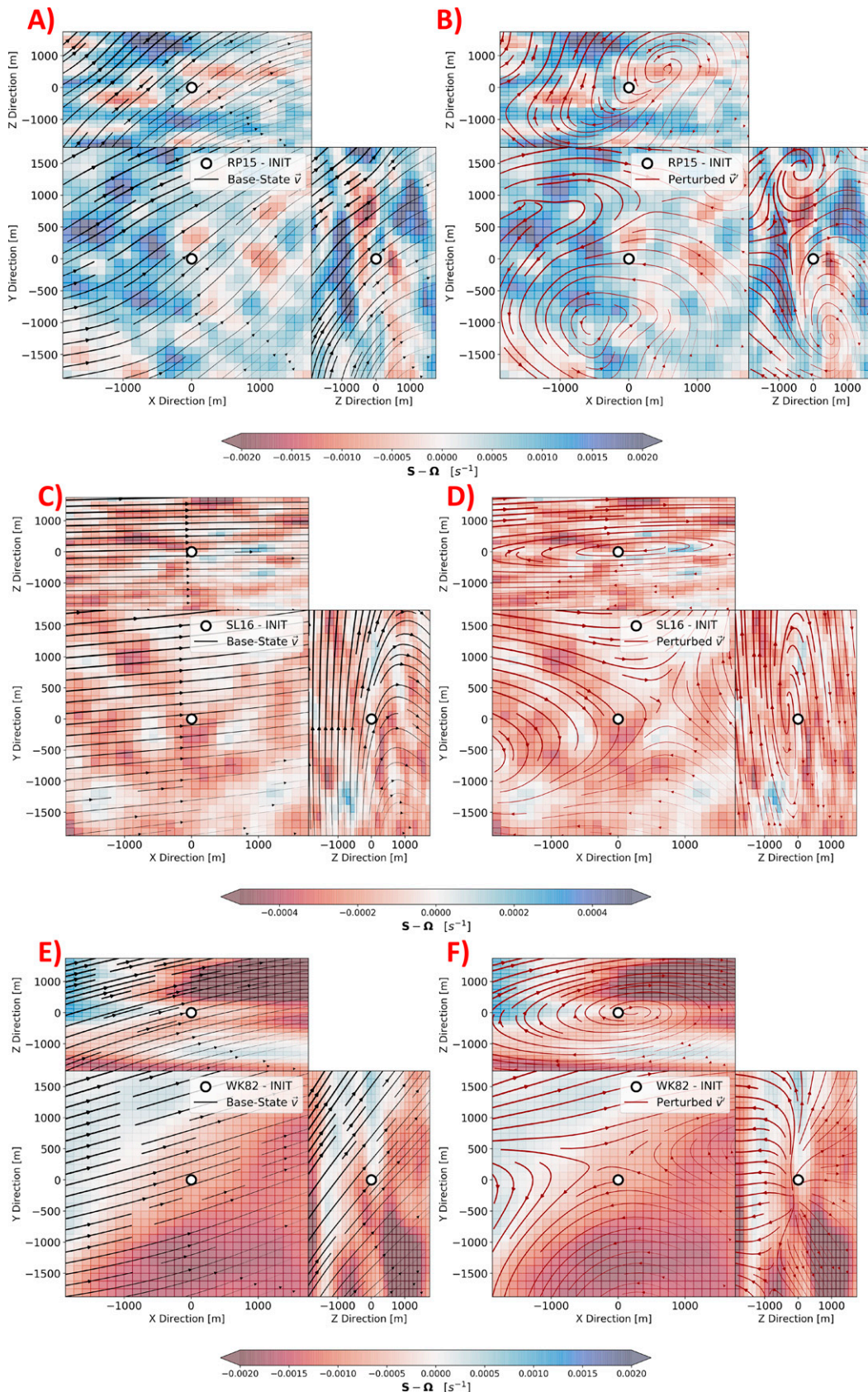


FIG. 9. Kinematic composites for (a),(b) RP15; (c),(d) SL16; and (e),(f) WK82. Base-state flow streamlines are illustrated in (a),(c),(e) for reference; and perturbed flow is illustrated in (b),(d),(f). Color fill is the difference between  $\|S\|$  and  $\|\Omega\|$  tensor norms derived from the perturbation storm velocity, where red and blue denote  $\|\Omega\|$  and  $\|S\|$  dominant flow, respectively; and a difference of zero is signified by white.

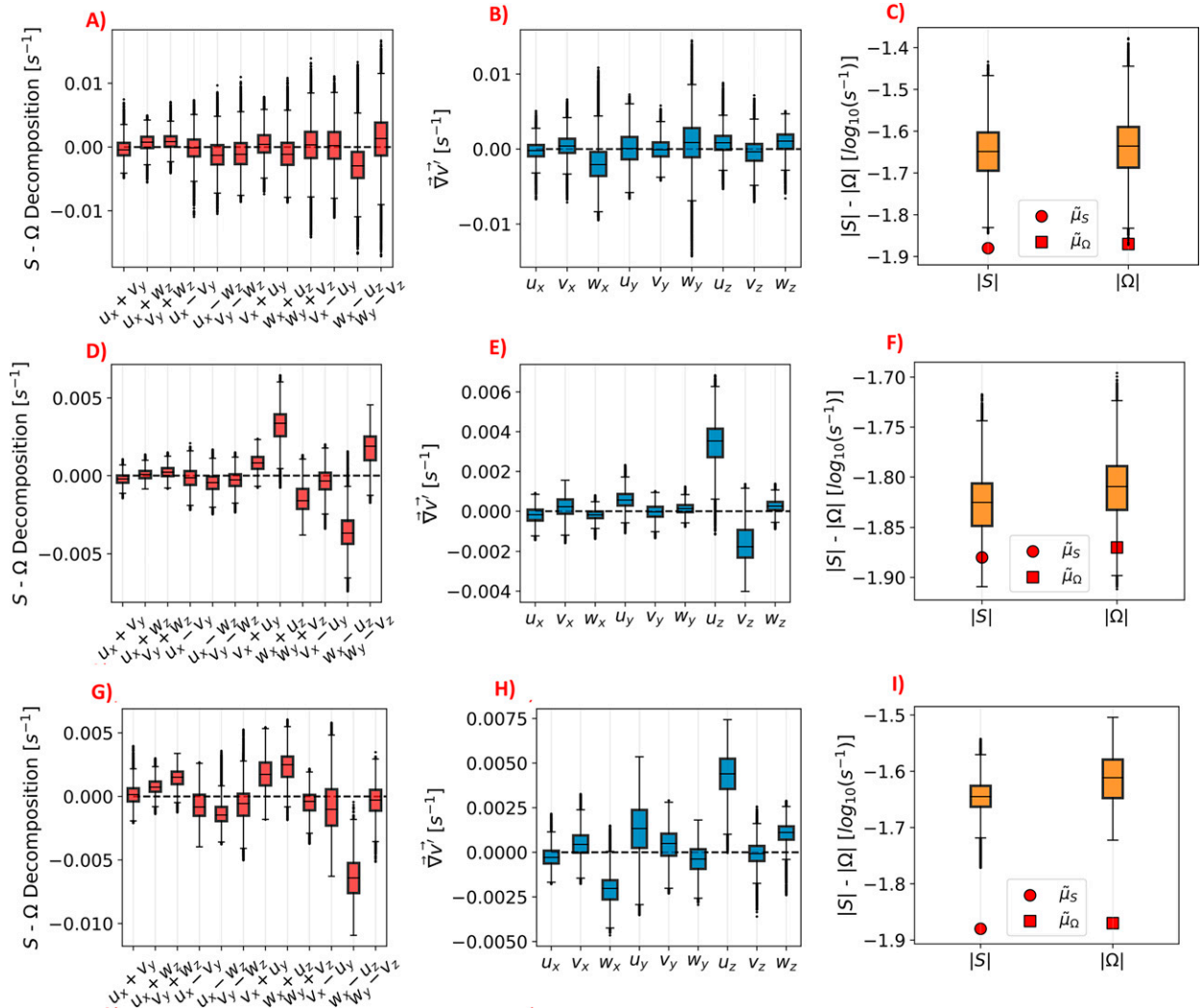


FIG. 10. Box-and-whisker distributions for the decomposition of the perturbation velocity gradient within the initiation volume for the average flash for (a)–(c) RP15, (d)–(f) SL16, and (g)–(i) WK82. (a),(d),(g) The velocity gradient in terms of vorticity, shearing, stretching, and divergence; (b),(e),(h) the individual velocity gradient components; and (c),(f),(i) the rate of strain and rotation within the initiation volumes where the red circle and square markers signify the median values found in the kinematic parameter space for each case.

addition, the decomposed kinematics for these composites (not shown) were found to be similar to those for all flashes (Fig. 10) so we only examine the flow structures as we may reference from our previous analysis which kinematic components dominated their formation.

The composite flow structures in the vertical dimensions for each case resembled those in Fig. 9 for flashes that initiated  $-60 \text{ s} < \Delta t$  before the pre-output times (Figs. 11a,e,i,m,q,u). For flashes that were initiated  $\Delta t < -60 \text{ s}$ , the flow structures were found to change slightly (Figs. 11b,f,j,n,r,v). For RP15, counterrotating vortices were found along the  $y$ - $z$  plane, with a single large vortex feature in the  $x$ - $z$  plane for all flashes in the pre-output subsets (Figs. 11a,b,e,f). The similar flow structures found for all flashes in the pre-output subset is likely due to a much slower ascending updraft given that it was a

much weaker storm, and so regardless of when flashes were initiated, the kinematic structures were similar at all times. For SL16, the flow structures along the  $x$ - $z$  and  $y$ - $z$  planes were similar to those for the entire flash population. However, changes in the flow structure in the  $y$ - $z$  plane were shown for flashes initiating  $\Delta t < 60 \text{ s}$  from the output time, while those in the  $x$ - $z$  plane remained similar. For WK82, however, flashes initiating  $-60 \text{ s} < \Delta t$  from the output time had a more consistent kinematic structure that was similar to that of RP15, and differed from what was found for all flashes (Figs. 11q,r,u,v). Flashes initiating  $\Delta t < -60 \text{ s}$  from the output time showed an entirely different flow structure in the  $y$ - $z$  plane. Note that these changes are due to flashes initiating in kinematic flow fields that have not yet been realized in the pre-output time, in other words, the output times at which the

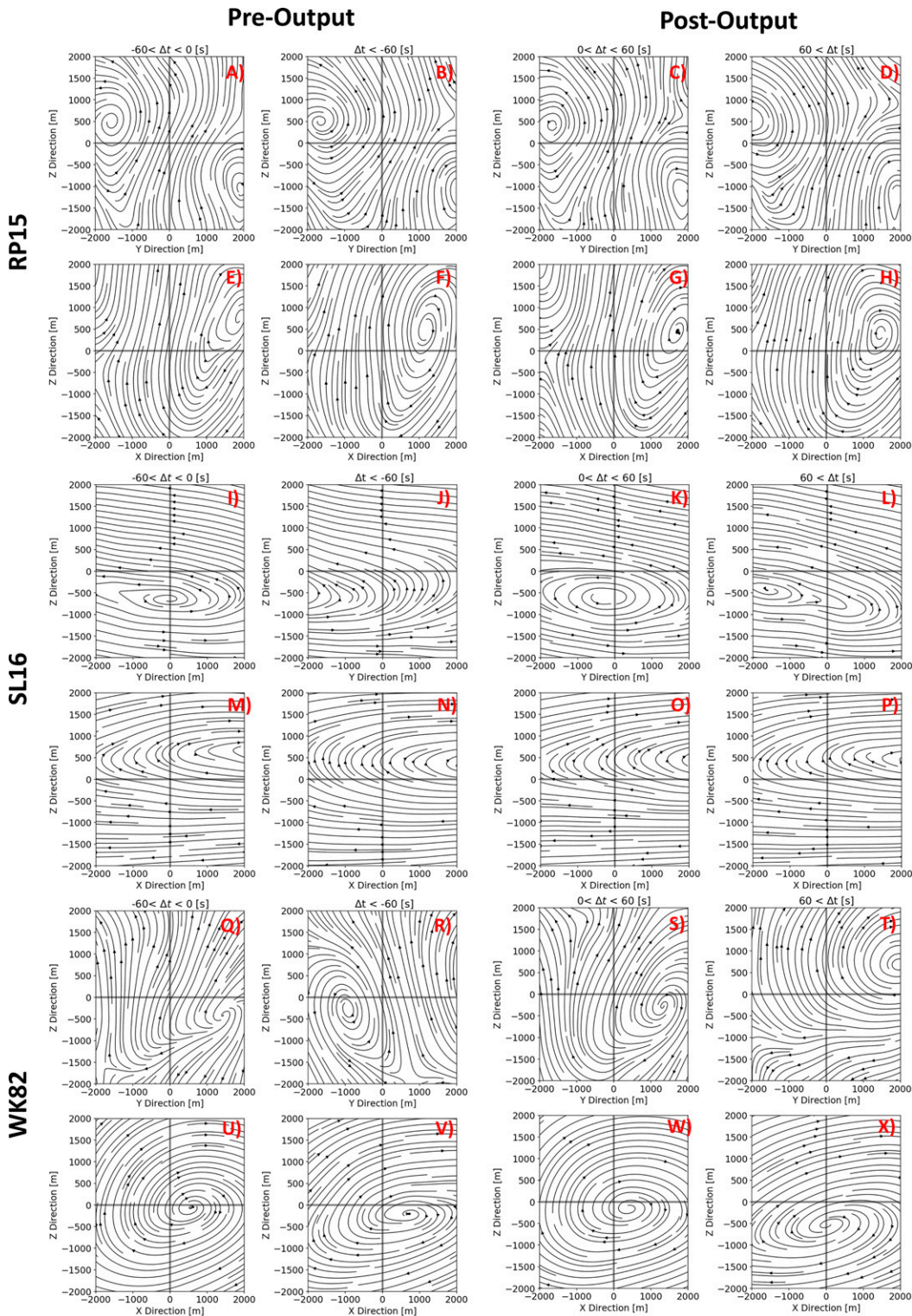


FIG. 11. Pre- and post-output initiation subset kinematic vertical  $x-z$  and  $y-z$  composites for the perturbed storm velocities for (a)–(h) RP15, (i)–(p) SL16, and (q)–(x) WK82. (a),(e),(i),(m),(q),(u) Flashes initiating with a time lag  $-60 \text{ s} < \Delta t$  from the pre-output time, and (b),(f),(j),(n),(r),(v) the flow composites for flashes initiating over  $60 \text{ s}$  after for the pre-output subsets. (c),(g),(k),(o),(s),(w) Flashes initiating with a time-lag  $\Delta t < 60 \text{ s}$  from the post-output time, and (d),(h),(l),(p),(t),(x) the flow composites for flashes initiating over  $60 \text{ s}$  after for the post-output subsets. In addition, the gray lines in all panels depict the 0 axes.

kinematics were sampled poorly depict the flow structures within which flashes with larger time lags ( $>60$  s) were initiated. Any similarities with flow structures for flashes initiating at times  $-60 \text{ s} < \Delta t$  from the pre-output time is due only to the close proximity of the initiations to one another within the output time storm environment, regardless of their exact initiation times.

### c. Post-output flashes

Composites for the post-output subsets were examined in the same way as those in the pre-output subsets. Flashes were separated depending on whether they were initiated with a  $\Delta t < 60$  s or  $\Delta t > 60$  s from the model-output time.

For all cases, flashes that were initiated within  $\Delta t < 60$  s of the post-output times had similar flow structures as those for the pre-output subsets (Figs. 11c,g,k,d,s,w). Flashes that were initiated with a  $60 \text{ s} < \Delta t$ , showed slight to large differences in the flow structures (Figs. 11d,h,l,p,t,x). For RP15, nearly identical flow structures were found in both  $x$ - $z$  and  $y$ - $z$  planes, while those initiating at  $60 \text{ s} < \Delta t$  showed subtle, yet noticeable differences (e.g., 1900 m along the  $y$  direction and  $-1000$  m along the  $z$  direction Fig. 11d). Similarly, the flow structure for SL16 was consistent with that of the pre-output subset for flashes initiating within 60 s, while those initiating after were different than their pre-output counterparts and whole flash populations. WK82 also showed a consistent flow structure for flashes initiating  $\Delta t < 60$  s from the output time, while showing a departure from any consistent flow patterns for flashes initiating  $>60$  s after.

## 7. Discussion

### a. Kinematics and electrostatics

Analysis of the initiation relative kinematics and electrostatics for all flashes and flash subsets revealed that the net charge tendency  $\rho_t$  and storm electric field  $E_{bg}$  either increased or decreased in magnitude with increases or decreases in magnitudes of strain and rotation flow. In other words, gradients from large-to-small or small-to-large values of  $\rho_t$  and  $E_{bg}$  were oriented with increases in  $\|\mathbf{S}\|$  and  $\|\mathbf{\Omega}\|$  magnitudes. In addition,  $\rho_t$  and  $E_{bg}$  were found to be largest in either strain or rotation dominant flow regimes, and lowest where they were equal. These results indicate that although the magnitude of the kinematics did not always match pattern increases or decreases with the initiation relative electrostatics, there tended to be a preference as to what flow regime the largest values of the net charge tendency and electric fields resided in.

Magnitudes of the electric potential were also found to vary similarly with the kinematics as found for  $\rho_t$  and  $E_{bg}$ . However,  $\phi_{bg}$  was found to vary less regardless of what flow regime a flash was initiated in, and its variation in relation to where it was sampled at an initiation location was within an order of magnitude. This result indicates that regardless of where or when flashes were initiated, the storm scale potential sampled at each initiation location was smaller (i.e., the

electrostatic energy integrated from the storm's whole charge structure was mostly the same from flash-to-flash and not strongly coupled to the local kinematic variability). For this reason,  $\rho_t$  can be inferred to have a significant impact on the generation of  $E_{bg}$  over  $\phi_{bg}$ , and its gradient alone, and suggests the importance of examining how  $\rho_t$  forms in reference to how the flow disperses charged hydrometeors, similar to the examination of the charge tendency and kinematics in Brothers et al. (2018).

That the largest initiation counts aligned where  $\|\mathbf{S}\| \approx \|\mathbf{\Omega}\|$ , also suggests where most flashes tend to initiate within a storm. Because the medians of  $\|\mathbf{S}\|$  and  $\|\mathbf{\Omega}\|$  were nearly equal, the individual flash initiation locations can be argued to be embedded in an interstitial flow regime between large scale rotation and strained dominant flow structures. The hypothesis of the present study is that most lightning flashes initiate between, or near, large overturning eddies generated along the periphery of strong strained vertical motion that is the convective updraft, and within such eddies, a wide zone of strain-rotation balance is expected as in an idealized thermal (Fig. 1).

The results of the initiation locations were also compared to randomly selected locations within the WK82 storm (not shown). The largest counts of these random locations also aligned within flow where  $\|\mathbf{S}\| \approx \|\mathbf{\Omega}\|$ ; however, the median magnitudes were much smaller (e.g.,  $10^{-2.16}$  and  $10^{-2.18}$  for  $\|\mathbf{S}\|$  and  $\|\mathbf{\Omega}\|$ , respectively), and the largest magnitudes of the randomly sampled locations were nearly equal to the medians at the individual initiation locations (Fig. 6). This result further suggests that where flashes were initiated resided within much stronger strain and rotational flow, which facilitated the charging and electric field generation needed to initiate them. The flow composites expanded upon the findings of this analysis to examine the average flow in which flashes were initiated, and if the kinematics were consistent across all cases.

### b. Flow structures

Lightning flashes were found to be initiated within similar composite flow structures across all cases, especially once the initiation time lag was carefully considered. In the vertical planes of the flow composites, vortical flow structures tended to dominate, and were found to form adjacent to strong upward vertical motion. Furthermore, the average flash was also found to initiate in a flow regime where  $\|\mathbf{S}\| \approx \|\mathbf{\Omega}\|$ , as shown by their difference being close to 0. The vertical composites are of most importance in this study as we desired to compare them to those of thermal bubbles, and found that RP15 had the best match as to what a thermal is typically depicted as. The average initiation along the  $y$ - $z$  plane for RP15 occurred near a region of vertical strained motion surrounded by counterrotating vortices on either side, similar to structure of toroidal circulations found on either side of a thermal core (Morrison and Peters 2018; Peters et al. 2019).

The pre- and post-output flashes were then considered to check for the consistency of these flow structures given that the initiation time lag affects the accuracy of the sampled

TABLE 4. The  $t$  test for composite  $\nabla\mathbf{v}$  components at initiation and random locations for WK82 ( $n = 4500$ ), SL16 ( $n = 9600$ ), and RP15 ( $n = 5700$ ).

$\nabla\mathbf{v}$	WK82		SL16		RP15	
	$t$	$p$ value	$t$	$p$ value	$t$	$p$ value
$u_x$	36.59	$3.14 \times 10^{-286}$	5.30	$1.12 \times 10^{-7}$	36.59	$3.14 \times 10^{-286}$
$u_y$	32.44	$1.56 \times 10^{-226}$	1.83	0.06	32.44	$1.56 \times 10^{-226}$
$u_z$	1.42	0.15	4.56	$5.04 \times 10^6$	1.42	0.15
$v_x$	51.52	0.00	2.78	0.005	51.52	0.00
$v_y$	32.17	$7.14 \times 10^{-223}$	5.24	$1.55 \times 10^{-7}$	32.17	$7.14 \times 10^{-223}$
$v_z$	18.15	$3.28 \times 10^{-73}$	4.44	$8.66 \times 10^{-6}$	18.15	$3.28 \times 10^{-73}$
$w_x$	54.21	0.00	4.78	$1.72 \times 10^6$	54.21	0.00
$w_y$	41.46	0.00	3.77	0.00	41.46	0.00
$w_z$	31.01	$1.76 \times 10^{-207}$	5.92	$3.32 \times 10^{-9}$	31.01	$1.76 \times 10^{-207}$
$\mathbf{S}$	885.29	0.00	46.15	0.00	631.03	0.00
$\mathbf{\Omega}$	907.66	0.00	245.313	0.00	681.01	0.00

kinematics they depict. In each subset, flashes initiating within a minute of either output time designation were nearly identical, and tended to match the structure of the flow identified using all flashes, with the exception of WK82. We argue here that the flow structures computed for the flash subsets for WK82 were better representative of the actual flow structures within which they were initiated, and thus the use of all flashes for WK82 led to some erroneous depictions of the flow patterns in which they were embedded due to the initiation time lag, whereas those initiating closest to the model output times showed a similar flow structure as that of RP15.

Our results here show that regardless of storm mode, or intensity, the average lightning flash tends to initiate in similar kinematic environments that are formed by nearly the same kinematic components as diagnosed by the velocity gradient, and are defined by horizontal vorticity and vertical shearing. The components of the velocity gradient responsible for forming these flow structures (horizontal gradients of vertical velocity and vertical gradients of horizontal velocity components) were found to be between a factor of 1.6–15 times larger than all other velocity gradient components thus confirming the dominance of the composite vortical flow structures. That all cases shared similar kinematic structures and dominant components is not simply coincidence, but reveals that the local accumulation of charge and the resulting breakdown electric fields are favored in these kinematic regions, and so subsequent studies should pay close attention to these regions in particular to conduct further analyses of how hydrometeors and charge are accumulated to support initiating lightning, in the vicinity of eddies, including thermal bubbles.

*c. Differences in kinematics: Flash-initiating versus non-flash-initiating environments*

The magnitudes of the velocity gradient components, and strain and rotation tensor norms, where lightning was initiated were compared to locations where their initiations were not favored. In doing so, it was possible to quantify the significance of how the magnitudes of the kinematic terms (i.e., the individual velocity gradient components and strain and rotation tensor norms) are always larger where the storm electrostatics

favored the initiation of lightning in comparison to elsewhere in the storm.

A  $t$  test was conducted to test whether magnitudes of the velocity gradient are always larger where flashes are initiated. The  $t$  test was chosen as the velocity gradient components with the largest magnitudes, and the magnitudes of the dominant shearing and vorticity components, were normally distributed (not shown). Locations where flashes were not initiated were randomly chosen within each storm throughout their entire durations. A total of 300 random samples were chosen for each time step for each storm to generate large sample populations. A total of 4500, 9700, and 5700 random samples were used for WK82, SL16, and RP15, respectively. Composites volumes, similar to the composite initiation volumes, for the kinematics at these random locations were then generated and used to directly compare the same kinematic components to those at the initiation locations. Table 4 summarizes the results of this analysis.

The  $t$  test confirmed that at locations where lightning is initiated the magnitudes of the kinematic components, namely the rate of strain and rotation tensor norms, are always significantly larger than where the electrostatic conditions to initiate lightning are not met. This is shown by values of  $t$ , or the  $t$  statistic, much greater than a value of 0 (e.g.,  $907 > t > 46$ ), and  $p$  values that were 0 (where the  $p$  value significance is determined by values  $< 0.05$ , or the 95th percentile of the distributions).

*d. Differences in the flow structure appearance*

The flow composites show that differences in the vertical flow structures exist from case-to-case (Fig. 11). These differences may be attributed to a variation in the vertical wind shear structure for each case, which determines the tilting of their updrafts and deforms the large eddy structures along their peripheries (Peters et al. 2019).

For SL16, the base-state kinematics surrounding the average initiated flash were dominated by vertical shearing components of  $u_z$  and  $v_z$  (Fig. 9c). The dominance of these shearing components acted to tilt the updraft (not shown) and in turn the local fluid motion. As a result, the eddies

generated along its periphery, as depicted by the vortical flow structures, appeared to be tilted and elongated (Fig. 9d) similar to those shown in (Peters et al. 2019) in environments with strong vertical wind shear. For WK82, strong vertical shearing was also present around the average initiated flash, which enabled the tilting of the updraft similar to SL16 (not shown). However, similar elongation of the vortical flow structures was not shown even though the 0–6-km bulk vertical wind shear was stronger (Fig. 9f). This difference between WK82 and SL16 vertical flow structures was attributed to the updraft of WK82 being less tilted due to components of the vertical  $u_z$  and horizontal  $w_x$  shearing dominating the flow environment of the storm (i.e.,  $w_x$  counters the elongation of the vortical flow structures in the horizontal and so they appear less deformed, Fig. 9d,f). For RP15, the updraft was much weaker than for the two supercell storms, as was its 0–6-km bulk vertical wind shear. As a result, the base state flow, and local kinematics, were shaped by dominant horizontal gradients of the vertical velocity component  $w_x$  and  $w_y$ , which resulted in formation of the symmetrically shaped vortical flow structures in the initiation composites similar to those computed in environments with no vertical wind shear in Peters et al. (2019) (Fig. 9b).

The differences in each storm's composite vertical flow structures are therefore considered to be a result of the structure of the updraft and the vertical shearing in the storm environment by which its shape is determined, as demonstrated by Peters et al. (2019). Differences in the flow structures within which the average flash is initiated should therefore vary from case-to-case, and storm mode, as a result of the dominant vertical wind shear direction and magnitude. Future work is recommended to examine these differences and their potential influence on how they impact the changes in a storm's electrification rate and rate of flash production that are known to vary by storm mode and intensity.

## 8. Summary and conclusions

Simulated lightning flashes embedded within large-eddy-resolving thunderstorm simulations were used in this study to examine the kinematic structures within which they are initiated, and how they corresponded to changes in the net charge tendency, electric field, and potential at their locations. Results of past work have shown that flashes are frequently initiated near the updraft (DiGangi et al. 2016), and the rate of flash production tends to follow increases in updraft velocity and volume through a storm's life cycle (Wiens et al. 2005; Deierling and Petersen 2008; Mecikalski et al. 2015). The results of this study now show that regions where flashes are initiated tend to be between or near large eddy structures and upward vertical ascent consistent with an updraft. These kinematic flow structures were found to be similar for two storm modes and two supercell storms of different convective strengths, and so we can infer that they illustrate a universal dynamical environment in which flashes are typically initiated.

Furthermore, that the electrostatics at locations where lightning was frequently initiated was a result of them being largely consumed after each time step when all flashes have terminated. These locations coincided with where strain and rotational flow were equal in magnitude, and suggest that where the electric field and charge is largely used up is near the convective updraft plume and between strain and rotation dominant flow structures where flashes are frequently initiated. The charge and electric fields in this flow regime are likely recovered quickly between flashes by how the kinematics locally organize charged hydrometeors; however, the model output depicts an environment immediately after the final flash in an output time step, and so these fields are shown to be small as a result of charge redistribution after a flash terminates (Mansell et al. 2002). Therefore, these lower magnitudes provide a footprint as to where flashes frequently initiated along a rising updraft in a thunderstorm.

The present study concludes that flashes are frequently initiated in similar flow structures within a storm that resemble those of a thermal bubble-like large eddies whose structures are defined by vertical straining motions that generate toroidal circulations along their periphery. That these flow structures were identified to surround the average initiated lightning flash implies that the fluid dynamics are in some way responsible for locally distributing and organizing charge into compact regions that support the generation of breakdown electric fields. A subsequent study will expand on the work herein, and will further explore how the electrostatics and precipitation microphysics at flash initiation, and within the initiation volumes, are related to the kinematics identified in this work. In addition, we recommend future work to examine this problem from a perspective that is focused on the updraft itself. Using the kinematics and kinematic structures identified in this study, it should be possible to examine how the fluid dynamics of a storm impacts the local organization of charged hydrometeors to generate the electric fields that are needed to initiate lightning.

*Acknowledgments.* The authors thank Drs. Johannes Dahl, and Christopher Weiss who helped improve the focus and narrative of this study. We would also like to thank Dr. Lisa Schielicke whose ideas and conversations inspired and shaped much of kinematic analysis methods, Matthew Brothers whose simulation runs have now been used for several studies, and to the anonymous reviewers for helping to improve this manuscript. This work is derived from the dissertation of Salinas (2020) and is funded by Grant NSF-AGS1352144.

*Data availability statement.* The data and analysis code used in this study are hosted on a private server, but may be made available upon request. Please contact the corresponding author if access to these data are desired.

## REFERENCES

Brothers, M. D., E. C. Bruning, and E. R. Mansell, 2018: Investigating the relative contributions of charge deposition and



- turbulence in organizing charge within a thunderstorm. *J. Atmos. Sci.*, **75**, 3265–3284, <https://doi.org/10.1175/JAS-D-18-0007.1>.
- Bruning, E. C., and D. R. MacGorman, 2013: Theory and observations of controls on lightning flash size spectra. *J. Atmos. Sci.*, **70**, 4012–4029, <https://doi.org/10.1175/JAS-D-12-0289.1>.
- , and R. J. Thomas, 2015: Lightning channel length and flash energy determined from moments of the flash area distribution. *J. Geophys. Res. Atmos.*, **120**, 8925–8940, <https://doi.org/10.1002/2015JD023766>.
- Bryan, G. H., J. C. Wyngaard, and J. M. Fritsch, 2003: Resolution requirements for the simulation of deep moist convection. *Mon. Wea. Rev.*, **131**, 2394–2416, [https://doi.org/10.1175/1520-0493\(2003\)131<2394:RRFTSO>2.0.CO;2](https://doi.org/10.1175/1520-0493(2003)131<2394:RRFTSO>2.0.CO;2).
- Calhoun, K. M., D. R. MacGorman, C. L. Ziegler, and M. I. Biggerstaff, 2013: Evolution of lightning activity and storm charge relative to dual-Doppler analysis of a high-precipitation supercell storm. *Mon. Wea. Rev.*, **141**, 2199–2223, <https://doi.org/10.1175/MWR-D-12-00258.1>.
- Dahl, J., 2020: Near-surface vortex formation in supercells from the perspective of vortex patch dynamics. *Mon. Wea. Rev.*, **148**, 3533–3547, <https://doi.org/10.1175/MWR-D-20-0080.1>.
- Damiani, R., G. Vali, and S. Haimov, 2006: The structure of thermals in cumulus from airborne dual-Doppler radar observations. *J. Atmos. Sci.*, **63**, 1432–1450, <https://doi.org/10.1175/JAS3701.1>.
- Deierling, W., and W. A. Petersen, 2008: Total lightning activity as an indicator of updraft characteristics. *J. Geophys. Res.*, **113**, D16210, <https://doi.org/10.1029/2007JD009598>.
- DiGangi, E., D. R. MacGorman, C. L. Ziegler, D. Betten, M. Biggerstaff, M. Bowlan, and C. K. Potvin, 2016: An overview of the 29 May 2012 Kingfisher supercell during DC3. *J. Geophys. Res. Atmos.*, **121**, 14316–14343, <https://doi.org/10.1002/2016JD025690>.
- Dwyer, J. R., 2005: The initiation of lightning by runaway air breakdown. *Geophys. Res. Lett.*, **32**, L20808, <https://doi.org/10.1029/2005GL023975>.
- Hernandez-Deckers, D., and S. C. Sherwood, 2016: A numerical investigation of cumulus thermals. *J. Atmos. Sci.*, **73**, 4117–4136, <https://doi.org/10.1175/JAS-D-15-0385.1>.
- Iudin, D. I., 2017: Lightning-discharge initiation as a noise-induced kinetic transition. *Radiophys. Quantum Electron.*, **60**, 374–394, <https://doi.org/10.1007/s11141-017-9807-x>.
- MacGorman, D. R., M. S. Elliott, and E. DiGangi, 2017: Electrical discharges in the overshooting tops of thunderstorms. *J. Geophys. Res. Atmos.*, **122**, 2929–2957, <https://doi.org/10.1002/2016JD025933>.
- Mansell, E. R., D. R. MacGorman, C. L. Ziegler, and J. M. Straka, 2002: Simulated three-dimensional branched lightning in a numerical thunderstorm model. *J. Geophys. Res.*, **107**, 4075, <https://doi.org/10.1029/2000JD000244>.
- , —, —, and —, 2005: Charge structure and lightning sensitivity in a simulated multicell thunderstorm. *J. Geophys. Res.*, **110**, D12101, <https://doi.org/10.1029/2004JD005287>.
- , C. L. Ziegler, and E. C. Bruning, 2010: Simulated electrification of a small thunderstorm with two-moment bulk microphysics. *J. Atmos. Sci.*, **67**, 171–194, <https://doi.org/10.1175/2009JAS2965.1>.
- Marshall, T. C., M. Stolzenburg, C. R. Maggio, L. M. Coleman, P. R. Krehbiel, T. Hamlin, R. J. Thomas, and W. Rison, 2005: Observed electric fields associated with lightning initiation. *Geophys. Res. Lett.*, **32**, L03813, <https://doi.org/10.1029/2004GL021802>.
- Mecikalski, R. M., A. L. Bain, and L. D. Carey, 2015: Radar and lightning observations of deep moist convection across northern Alabama during DC3: 21 May 2012. *Mon. Wea. Rev.*, **143**, 2774–2794, <https://doi.org/10.1175/MWR-D-14-00250.1>.
- Mitzeva, R. P., C. P. R. Saunders, and B. Tsenova, 2005: A modelling study of the effect of cloud saturation and particle growth rates on charge transfer in thunderstorm electrification. *Atmos. Res.*, **76**, 206–221, <https://doi.org/10.1016/j.atmosres.2004.11.019>.
- Morrison, H., and J. M. Peters, 2018: Theoretical expressions for the ascent rate of moist deep convective thermals. *J. Atmos. Sci.*, **75**, 1699–1719, <https://doi.org/10.1175/JAS-D-17-0295.1>.
- Okubo, A., 1970: Horizontal dispersion of floatable particles in the vicinity of velocity singularities such as convergences. *Deep-Sea Res.*, **17**, 445–454, [https://doi.org/10.1016/0011-7471\(70\)90059-8](https://doi.org/10.1016/0011-7471(70)90059-8).
- Peters, J. M., W. Hannah, and H. Morrison, 2019: The influence of vertical wind shear on moist thermals. *J. Atmos. Sci.*, **76**, 1645–1659, <https://doi.org/10.1175/JAS-D-18-0296.1>.
- Rakov, V. A., and M. A. Uman, 2003: *Lightning Physics and Effects*. Cambridge University Press, 687 pp.
- Reynolds, S. E., M. Brook, and M. F. Gourley, 1957: Thunderstorm charge separation. *J. Meteor.*, **14**, 426–436, [https://doi.org/10.1175/1520-0469\(1957\)014<0426:TCS>2.0.CO;2](https://doi.org/10.1175/1520-0469(1957)014<0426:TCS>2.0.CO;2).
- Rison, W., P. R. Krehbiel, M. G. Stock, H. E. Edens, X.-M. Shao, R. J. Thomas, M. Stanley, and Y. Zhang, 2016: Observations of narrow bipolar events reveal how lightning is initiated in thunderstorms. *Nat. Commun.*, **7**, 10721, <https://doi.org/10.1038/ncomms10721>.
- Romps, D. M., and A. B. Charn, 2015: Sticky thermals: Evidence for a dominant balance between buoyancy and drag in cloud updrafts. *J. Atmos. Sci.*, **72**, 2890–2901, <https://doi.org/10.1175/JAS-D-15-0042.1>.
- Salinas, V., 2020: Examining thunderstorm kinematic structures in which lightning initiates and how the causal electrostatics are generated. Ph.D. dissertation, Texas Tech University, 244 pp.
- Saunders, C., 2008: Charge separation mechanisms in clouds. *Space Sci. Rev.*, **137**, 335–353, <https://doi.org/10.1007/s11214-008-9345-0>.
- , and S. L. Peck, 1998: Laboratory studies of the influence of the rime accretion rate on charge transfer during crystal/graupe collisions. *J. Geophys. Res.*, **103**, 13 949–13 956, <https://doi.org/10.1029/97JD02644>.
- Schielicke, L., P. Névir, and U. Ulbrich, 2016: Kinematic vorticity number—A tool for estimating vortex sizes and circulations. *Tellus*, **68A**, 29464, <https://doi.org/10.3402/tellusa.v68.29464>.
- Schultz, C. J., and Coauthors, 2015: Insight into the kinematic and microphysical processes that control lightning jumps. *Wea. Forecasting*, **30**, 1591–1621, <https://doi.org/10.1175/WAF-D-14-00147.1>.
- Simpson, G., and F. J. Scrase, 1937: The distribution of electricity in thunderclouds. *Proc. Roy. Soc. London*, **161**, 309–352, <https://doi.org/10.1098/rspa.1937.0148>.
- Stolzenburg, M., W. D. Rust, and T. C. Marshall, 1998: Electrical structure in thunderstorm convective regions 3. Synthesis. *J. Geophys. Res.*, **103**, 14 097–14 108, <https://doi.org/10.1029/97JD03545>.
- Takahashi, T., 1978: Riming electrification as a charge generation mechanism in thunderstorms. *J. Atmos. Sci.*, **35**, 1536–1548, [https://doi.org/10.1175/1520-0469\(1978\)035<1536:REAACG>2.0.CO;2](https://doi.org/10.1175/1520-0469(1978)035<1536:REAACG>2.0.CO;2).
- Ushio, T., S. J. Heckman, H. J. Christian, and Z.-I. Kawasaki, 2003: Vertical development of lightning activity observed

- by the LDAR system: Lightning bubbles. *J. Appl. Meteor.*, **42**, 165–174, [https://doi.org/10.1175/1520-0450\(2003\)042<0165:VDOLAO>2.0.CO;2](https://doi.org/10.1175/1520-0450(2003)042<0165:VDOLAO>2.0.CO;2).
- Weisman, M. L., and J. B. Klemp, 1982: The dependence of numerically simulated convective storms on vertical wind shear and buoyancy. *Mon. Wea. Rev.*, **110**, 504–520, [https://doi.org/10.1175/1520-0493\(1982\)110<0504:TDOMNSC>2.0.CO;2](https://doi.org/10.1175/1520-0493(1982)110<0504:TDOMNSC>2.0.CO;2).
- Wicker, L. J., and R. B. Wilhelmson, 1995: Simulation and analysis of tornado development and decay within a three-dimensional supercell thunderstorm. *J. Atmos. Sci.*, **52**, 2675–2703, [https://doi.org/10.1175/1520-0469\(1995\)052<2675:SAOTD>2.0.CO;2](https://doi.org/10.1175/1520-0469(1995)052<2675:SAOTD>2.0.CO;2).
- Wiens, K. C., S. A. Rutledge, and S. A. Tessendorf, 2005: The 29 June 2000 supercell observed during the STEPS. Part II: Lightning and charge structure. *J. Atmos. Sci.*, **62**, 4151–4177, <https://doi.org/10.1175/JAS3615.1>.
- Williams, E. R., 1985: Large-scale charge separation in thunderclouds. *J. Geophys. Res.*, **90**, 6013–6025, <https://doi.org/10.1029/JD090iD04p06013>.
- , and R. M. Lhermitte, 1983: Radar tests of the precipitation hypothesis for thunderstorm electrification. *J. Geophys. Res.*, **88**, 10 984–10 992, <https://doi.org/10.1029/JC088iC15p10984>.
- Wilson, C. T. R., 1921: Investigations on lightning discharges and on the electric field of thunderstorms. *Philos. Trans. Roy. Soc. London*, **A221**, 73–115, <https://doi.org/10.1098/rsta.1921.0003>.